Int. J. Solids Structures Vol. 21, No. 3, pp. 279–293, 1985
Printed in the U.S.A.

0020-7683/85 $3.00 + .00

INFLUENCE OF GRAIN BOUNDARY SLIDING ON MATERIAL FAILURE IN THE TERTIARY CREEP RANGE

VIGGO TVERGAARD
Department of Solid Mechanics, The Technical University of Denmark, Lyngby, Denmark

(*Received* 13 *February* 1984)

Abstract—In the later stages of a creep rupture process, a number of micro-cracks form at grain boundary facets normal to, or nearly normal to, the maximum principal tensile stress. Then the grains can be pulled apart by a mechanism involving grain boundary sliding together with dislocation creep of the grains. An axisymmetric model problem is formulated, by which some features of this final separation process can be studied, and the model is analysed numerically. Free sliding on the grain boundaries is assumed, and different boundary conditions are used in the analyses to simulate a variety of situations. The calculated times for separation by this process of grain boundary sliding are compared with times required for cavitation on grain boundary facets.

1. INTRODUCTION

Creep rupture in polycrystalline metals at high temperatures tends to occur as intergranular fracture. This type of failure begins by the formation of small grain boundary voids, which grow by diffusion as well as by dislocation creep of the surrounding material (see Needleman and Rice[1], Cocks and Ashby[2], Sham and Needleman[3]). When the cavities on a grain boundary facet have grown to coalescence, a micro-crack is formed, and finally failure occurs as such micro-cracks link up.

Creep experiments show that cavitation occurs mainly on grain boundary facets normal to the maximum principal tensile stress direction (Hull and Rimmer[4], Trampczynski *et al.*[5], Dyson *et al.*[6]). The time interval from the moment at which the cavities nucleate on a facet until they link up is often a significant part of the material's lifetime. As noted by Dyson[7], the cavity growth rate determining this rupture time is constrained by the creep rate of the surrounding grains. The increase of the creep rupture time for a grain facet, due to the creep constraint on diffusive cavity growth, has been estimated by Rice[8]. In cases where creep growth of cavities plays a role, as well as diffusive growth, rupture times for grain boundary facets have recently been calculated by Tvergaard[9].

Grain boundary sliding gives a significant contribution to the total strain in most polycrystalline metals at elevated temperatures. Sliding at a boundary involves diffusive motion of atoms, accompanied by a migration of the boundary, as has been described by Ashby[10]. Modelling this atom flow leads to a linearly viscous expression for the shear stress along the grain boundary in terms of the rate of sliding. Grain boundary sliding can be markedly reduced by introducing alloying elements, which form concentrated solutions or precipitates at the grain boundary[10, 11]. The effect of grain boundary sliding on steady-state creep in polycrystalline metals has been analysed numerically by Crossman and Ashby[12] and Ghahremani[13], with the deformations inside the grains represented as power law creep, and grain boundary sliding represented as linearly viscous.

With an increasing density of micro-cracks formed by cavitation on grain boundary facets normal to the maximum principal tensile stress direction, the steady-state creep behaviour is gradually replaced by tertiary creep, where the macroscopic strain rates keep increasing. At this stage, the failure process can proceed by cavity growth on adjacent grain boundaries inclined to the maximum principal stress, by a mechanism that mainly relies on the opening of the microcracks due to grain boundary sliding, or by a combination of these mechanisms.

In the present study, the grain boundary sliding mechanism of final failure will be investigated by calculating rupture times for various model problems. In these model problems it will be assumed that shear stresses on the grain boundaries relax so rapidly that sliding can be considered completely free (zero viscosity), and since creep deformations of the grains are necessary to pull them apart by sliding at the boundaries, the rupture time is determined by the rate of creep inside the grains. One motivation for calculating these times is that the mechanism analysed is an integral part of tertiary creep, and that in some materials the tertiary creep stage represents a significant portion of the total lifetime. Knowing the times required for this kind of failure, it is possible to roughly identify the circumstances in which failure by cavitation on the grain boundaries considered would precede failure by sliding off.

2. PROBLEM FORMULATION

The axisymmetric model problem illustrated in Fig. 1(a) is used to study some of the effects involved in pulling grains apart by grain boundary sliding. The initial stage in this analysis is taken to be the situation where a micro-crack with radius R_0 has just been formed by coalescence of cavities. One half grain is represented by the truncated cone emanating from the edges of the micro-crack, and the external ring of material is taken to represent a number of grains surrounding the central grain of the model. Since free grain boundary sliding is assumed, the central grain is only kept attached to the surrounding ring of material by normal stresses on the conical grain boundary.

This axisymmetric model is mainly designed to study the interaction between the central grain and the surrounding material. The model is not able to give a detailed representation of the grains in the external ring of material, but it will be assumed that some of the axial load is transmitted directly through the external ring, so that only part of the load on the region analysed has to be carried by the normal stresses on the conical grain boundary.

The initial geometry of the model is specified by the radius A_0 and the height B_0, which are taken to represent characteristic spacings between open micro-cracks in the material. The initial dimensions of the central grain are given by the radius R_0 of the facet at the open micro-crack and the radius C_0 in the central cross-section of the grain. In the cylindrical reference coordinate system shown in Fig. 1(a) the axial coordinate, the radius and the circumferential angle are denoted by x^1, x^2 and x^3, respectively. The displacement components on the reference base vectors are u^i and the nominal traction components on a surface are denoted by T^i.

The boundary conditions used in most of the calculations to be presented are

$$T^1 = T^2 = T^3 = 0, \quad \text{at } x^1 = 0,\ 0 \le x^2 \le R_0 \tag{2.1}$$

$$u^1 = 0,\ T^2 = T^3 = 0, \quad \text{at } x^1 = 0,\ R_0 \le x^2 \le A_0 \tag{2.2}$$

$$u^2 = U_{\mathrm{II}},\ T^1 = T^3 = 0, \quad \text{at } 0 \le x^1 \le B_0,\ x^2 = A_0 \tag{2.3}$$

$$u^1 = U_{\mathrm{I}},\ T^2 = T^3 = 0, \quad \text{at } x^1 = B_0,\ 0 \le x^2 \le C_0 \tag{2.4}$$

$$u^1 = U_{\mathrm{III}},\ T^2 = T^3 = 0, \quad \text{at } x^1 = B_0,\ C_0 \le x^2 \le A_0. \tag{2.5}$$

The three constants U_{I}, U_{II}, and U_{III} are displacements illustrated in Fig. 1(b). The values of these displacements at a given time are determined such that the average true stresses σ_1 and σ_2 in the axial and radial direction, respectively, are as specified. Corresponding to the three displacements U_{I}, U_{II} and U_{III}, three forces are defined by

$$F_{\mathrm{I}} = 2\pi \int_0^{C_0} [T^1 x^2]_{x^1 = B_0}\, \mathrm{d}x^2, \qquad F_{\mathrm{II}} = 2\pi A_0 \int_0^{B_0} [T^2]_{x^2 = A_0}\, \mathrm{d}x^1$$
$$F_{\mathrm{III}} = 2\pi \int_{C_0}^{A_0} [T^1 x^2]_{x^1 = B_0}\, \mathrm{d}x^2 \tag{2.6}$$

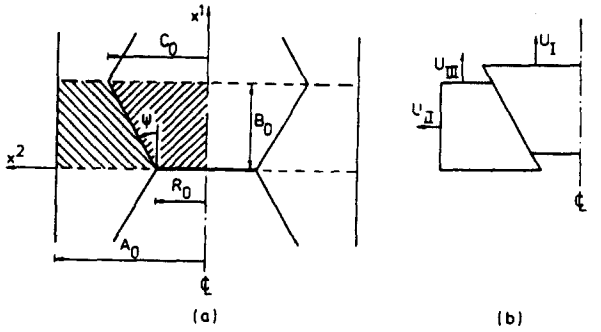

Fig. 1. Axisymmetric model problem. The grain boundary facet with radius R_0 is an open micro-crack, and only the hatched region is analysed.

and in terms of these forces, the average true stresses are given by

$$\sigma_1 = (F_I + F_{III})(\pi A^2)^{-1}, \qquad \sigma_2 = F_{II}(2\pi AB)^{-1} \tag{2.7}$$

where $A = A_0 + U_{II}$ and $B = B_0 + U_I$ are the current radius and height, respectively, of the region analysed. The load resulting in the stresses σ_1 and σ_2 is applied at the initial stage (at time $t = 0$), and subsequently these average stresses are kept fixed.

The uniform displacement U_{III} on the top of the external ring of material is used to approximate the average effect of having some micro-cracks at the top facets of the surrounding grains (if there were no micro-cracks here, $U_{III} = U_I$ should be specified, whereas $U_{III} < U_I$ is expected if some of these grain boundaries have cracked). The force F_{III} is taken to be

$$F_{III} = \alpha F_I \tag{2.8}$$

so that the value of the parameter α gives an indication of the degree of cracking on the top of these surrounding grains ($\alpha = 0$ if all the top of the external ring is part of an open crack).

The freely sliding behaviour at the grain boundary is described approximately in terms of a layer of linear elastic springs. Thus, tangential stresses on the sliding surfaces are neglected and the true stress σ_n normal to the current orientation of the grain boundary is taken to be

$$\sigma_n = kd \tag{2.9}$$

where d is the distance between the surfaces of the two grains sliding against one another, and k is the spring stiffness. Allowing for a non-zero distance d gives an inaccuracy, which is kept very small by using a large stiffness k. Here, the stiffness $k = 6.67\, E/A_0$ (where E is Young's modulus) is found sufficiently large to obtain a good approximation by (2.9).

Continuity of the displacements in the direction normal to the sliding grain boundary should actually be prescribed, rather than the fictitious springs (2.9). However, in the numerical solution (see Section 3) the two sides of the sliding boundary are described as piecewise linear, and with this assumption, continuity of the normal displacements would not permit any curvature of the grain boundary, except when nodal points are exactly opposite one another. Such unrealistic constraints are avoided by using (2.9), with a reasonable choice of the stiffness k.

The material inside the grains is taken to deform by power law creep in addition to elastic deformations. Pulling the grains apart by grain boundary sliding gives rise to large strains, which are accounted for in the Lagrangian formulation of the field equations to be employed here.

The Lagrangian strain, in terms of the displacement components u^i on the reference base vectors, is given by

$$\eta_{ij} = \tfrac{1}{2}(u_{i,j} + u_{j,i} + u^k_{,i}u_{k,j}) \tag{2.10}$$

where $(\ )_{,i}$ denotes covariant differentiation in the reference frame, indices range from 1 to 3, and the summation convention is adopted for repeated indices. The contravariant components τ^{ij} of the Kirchhoff stress tensor on the embedded deformed coordinates are defined in terms of the Cauchy stress tensor σ^{ij} by

$$\tau^{ij} = \sqrt{G/g}\,\sigma^{ij} \tag{2.11}$$

where G and g are the determinants of the metric tensors G_{ij} and g_{ij} in the current configuration and in the reference configuration, respectively.

The steady creep behaviour of the material inside the grain is taken to follow Norton's law, generalized to multiaxial stress states[14]

$$\dot{\eta}^C_{ij} = \frac{3}{2}\,\dot{\epsilon}_0 \left(\frac{\sigma_e}{\sigma_0}\right)^{n-1} \frac{s_{ij}}{\sigma_0} \tag{2.12}$$

where $\dot{\epsilon}_0$ and σ_0 are reference strain-rate and stress quantities, n is the creep exponent, and $\dot{(\ )}$ denotes differentiation with respect to time. The stress deviator $s^{ij} = \tau^{ij} - G^{ij}\tau^k_k/3$ and the effective Mises stress $\sigma_e = (3s_{ij}s^{ij}/2)^{1/2}$ are specified in terms of Kirchhoff stresses, since the elastic volume changes are small (see discussion in [9]).

The total strain-rate $\dot{\eta}_{ij}$ is taken to be the sum of the elastic part $\dot{\eta}^E_{ij}$ and the creep part $\dot{\eta}^C_{ij}$, with the elastic part given by

$$\dot{\eta}^E_{ij} = \frac{1}{E}\{(1+\nu)G_{ik}G_{jl} - \nu G_{ij}G_{kl}\}\overset{\nabla}{\tau}{}^{kl}. \tag{2.13}$$

Here, E is Young's modulus, ν is Poisson's ratio, and $\overset{\nabla}{\tau}{}^{kl}$ is the Jaumann rate of the Kirchhoff stress tensor

$$\overset{\nabla}{\tau}{}^{kl} = \dot{\tau}^{kl} + (G^{kr}\tau^{ls} + G^{lr}\tau^{ks})\dot{\eta}_{rs}. \tag{2.14}$$

The inverse of the elastic relationship (2.13) is written as $\overset{\nabla}{\tau}{}^{ij} = \mathcal{R}^{ijkl}\dot{\eta}^E_{kl}$, with $\mathcal{R}^{ijkl}$ denoting the elastic instantaneous moduli, and thus the constitutive relations accounting for creep are of the form

$$\overset{\nabla}{\tau}{}^{ij} = \mathcal{R}^{ijkl}(\dot{\eta}_{kl} - \dot{\eta}^C_{kl}). \tag{2.15}$$

The average value of the normal stress σ_n on the conical grain boundary (in the initial stage) is directly given by equilibrium in the axial direction

$$(\sigma_n)_{av} = \frac{F_1}{\pi(C_0^2 - R_0^2)}. \tag{2.16}$$

The stress level and thus the creep rate in the model problem are much affected by the value of this average stress. Therefore, it is important to note that this stress value is strongly sensitive to the angle of inclination ψ of the conical grain boundary, with $(\sigma_n)_{av} \to \infty$ for $\psi \to 0$.

3. NUMERICAL METHOD

A linear incremental method is used to solve the axisymmetric model problem illustrated in Fig. 1(a). The equations governing the stress increments $\Delta\tau^{ij} = \dot{\tau}^{ij}\Delta t$, the strain increments $\Delta\eta_{ij} = \dot{\eta}_{ij}\Delta t$, etc. during the time increment Δt are obtained by expanding the principle of virtual work about the current state, using (2.10). To the lowest order the incremental equation is

$$\int_V \{\Delta\tau^{ij}\delta\eta_{ij} + \tau^{ij}\Delta u^k_{,i}\delta u_{k,j}\}\,dV = \int_S \Delta T^i\delta u_i\,dS - \left[\int_V \tau^{ij}\delta\eta_{ij}\,dV - \int_S T^i\delta u_i\,dS\right] \tag{3.1}$$

where V and S are the volume and surface, respectively, of the body in the reference configuration, and the terms bracketed in (3.1) are included to prevent drifting of the solution away from the true equilibrium path.

The incremental equation (3.1) includes contributions from the layer of springs (2.9) used to approximate the freely sliding behaviour at the grain boundary, although these terms are not specifically written out.

The mesh used in the incremental finite-element solution consists of quadrilaterals, each built up of four linear displacement triangular elements. Most calculations are carried out with 8 × 6 quadrilaterals in the central grain and 8 × 6 quadrilaterals in the surrounding ring of material. For a case with $B_0/A_0 = 0.577$, $R_0/A_0 = 0.333$ and $C_0/A_0 = 0.667$ (and thus $\psi = 30°$) the initial mesh is shown in Fig. 2. A few calculations were carried out with a cruder mesh (4 × 3 and 4 × 3 quadrilaterals), which gave good agreement with strain rates found by the finer mesh at the earlier part of the process, but slightly higher total rupture times. On this basis the mesh in Fig. 2 is considered sufficient for the present analyses.

It is noted that the nodal points on each side of the conical grain boundary surface coincide in Fig. 2; but subsequently these nodal points slide along the elements on the opposite side of the grain boundary. In each increment the layer of springs (2.9) is represented in terms of special finite elements along the grain boundary.

A forward gradient method proposed by Peirce *et al.*[15] is used to increase the stable step size in the incremental solution. The basic idea in this method is to express the effective creep strain rate, $\dot{\epsilon}^C = \dot{\epsilon}_0(\sigma_e/\sigma_0)^n$, by a linear interpolation between the rates at time t and $t + \Delta t$, respectively, using a Taylor series expansion to estimate the value of the rate at time $t + \Delta t$. The equations resulting from this procedure have been given in [9] and shall not be repeated here.

The boundary conditions specified in terms of (2.1)–(2.8), for prescribed average true stresses σ_1 and σ_2, are enforced in the numerical solution by application of a mixed finite-element/Rayleigh Ritz method (see also [9, 16]).

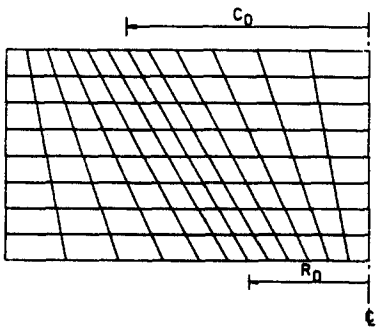

Fig. 2. Typical mesh used in numerical analyses.

4. RESULTS

Numerical results will be presented here mainly in the form of diagrams showing the average logarithmic strains $\epsilon_1 = \ln(1 + U_1/B_0)$ and $\epsilon_2 = \ln(1 + U_{II}/A_0)$ versus time. All times are normalized by a reference time $t_R = \sigma_e/(E\dot{\epsilon}_e^C)$, where $\sigma_e = |\sigma_1 - \sigma_2|$ is the average effective Mises stress and $\dot{\epsilon}_e^C = \dot{\epsilon}_0(\sigma_e/\sigma_0)^n$ is the corresponding effective creep strain-rate. In all cases considered the creep exponent is taken to be $n = 5$, Poisson's ratio is $\nu = \frac{1}{3}$ and $B_0/A_0 = 0.577$. Then, in most of the cases, where $R_0/A_0 = 0.333$ and $C_0/A_0 = 0.667$ are used, the cone angle is $\psi = 30°$.

In Fig. 3 the average true stresses are specified by $\sigma_1/E = 4 \cdot 10^{-4}$ and $\sigma_2/\sigma_1 = \frac{1}{2}$, so that the average effective Mises stress is $\sigma_e/E = 2 \cdot 10^{-4}$. In (2.8) the value $\alpha = 1$ is assumed, indicating a rather high degree of cracks on the top of the grains modelled by the external ring of material. The cone angle is $\psi = 30°$, with $R_0/A_0 = 0.333$ and $C_0/A_0 = 0.667$.

Figure 3 shows that the rate of growth of ϵ_1 is rather constant in a wide intermediate range of the process. Just before final failure, this strain-rate increases strongly, as the grains are pulled apart. On the other hand, the rate of change of the average radial strain ϵ_2 remains nearly constant throughout the whole process, with no significant changes near the point of final failure. The decaying strain-rates in the initial stage result from geometry changes and from a relaxation of elastic stress peaks that differ from the stress distribution in the steady state. One of the geometry effects is that the rate of radial contraction of the external ring of material decays, as the radius decreases and the cross-sectional area increases.

Figure 4 shows deformed meshes at four different stages, $\epsilon_1 = 0.010$, $\epsilon_1 = 0.245$, $\epsilon_1 = 0.414$ and $\epsilon_1 = 0.586$, of the creep curves illustrated in Fig. 3. In the early stages the macroscopic deformations result mainly from compressive hoop strains in the external ring of material that is pulled in to a smaller radius by the normal stresses on the sliding grain boundary. This mode of deformation is counteracted by the prescribed external radial stress σ_2, so that a higher value of σ_2 would slow down the creep process. The final stage, at which the creep-rate $\dot{\epsilon}_1$ grows very large, is just about to begin in Fig. 4(c) and Fig. 4(d) shows that this final stage is characterized by more local deformations near the remaining contact area on the conical grain boundary. It is noted from Fig. 4(c) that the grains are still only half separated at a stage where nearly all the lifetime has gone.

In Figs. 5 and 6 the same analysis is repeated for $\alpha = 3$ and $\alpha = 0$, corresponding to fewer micro-cracks on the top of the surrounding ring of grains or to a completely cracked top, respectively. From (2.16) it is seen that, relative to Fig. 3, the average normal stress $(\sigma_n)_{av}$ on the conical grain boundary is divided by 2 in Fig. 5 and multiplied by 2 in Fig. 6. Thus, if the stress level is mainly determined by $(\sigma_n)_{av}$, the strain-rates should be divided or multiplied by $2^n = 32$ in the two figures, and the rupture times should be multiplied or divided by 2^n. In fact the ratios between the rupture times in Figs. 3, 5 and 6 are not exactly 2^n, but the order of magnitude is right.

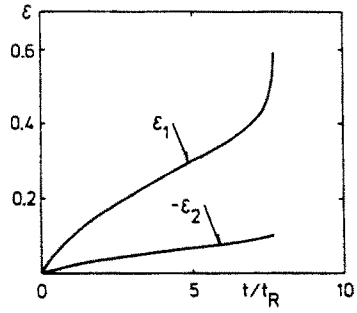

Fig. 3. Average logarithmic strains vs. time for $\alpha = 1$, $\sigma_1/E = 4 \cdot 10^{-4}$, $\sigma_2/\sigma_1 = 0.5$ and $\psi = 30°$.

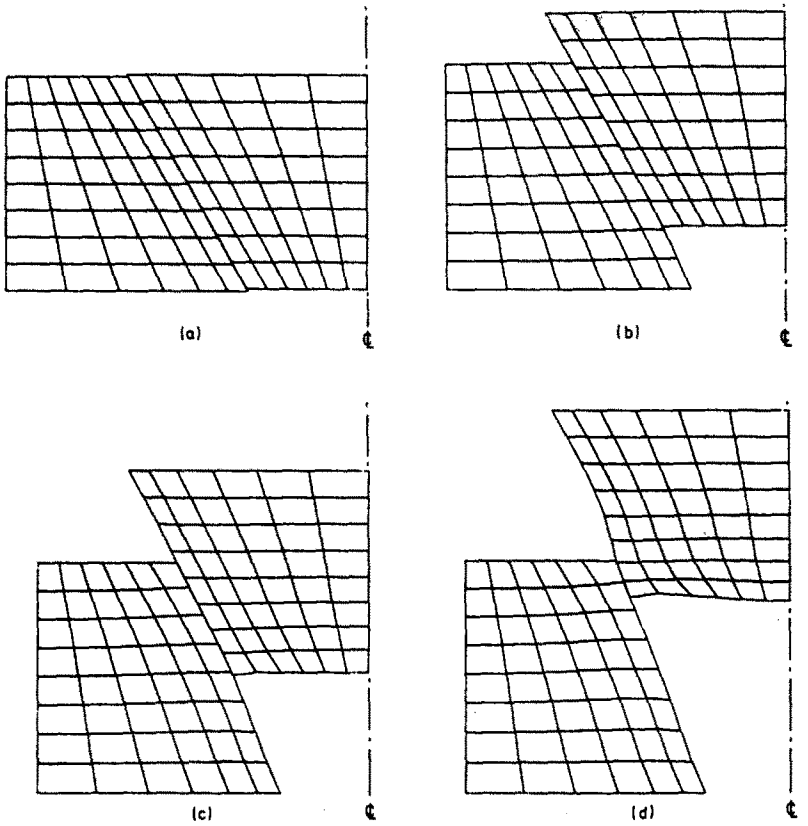

Fig. 4. Deformed meshes corresponding to $\alpha = 1$, $\sigma_1/E = 4 \cdot 10^{-4}$, $\sigma_2/\sigma_1 = 0.5$ and $\psi = 30°$. (a) $\epsilon_1 = 0.010$, (b) $\epsilon_1 = 0.245$, (c) $\epsilon_1 = 0.414$, (d) $\epsilon_1 = 0.586$.

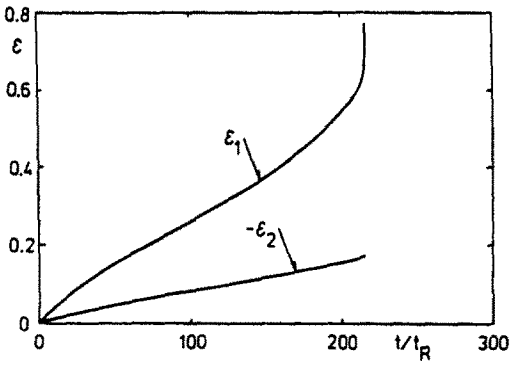

Fig. 5. Average logarithmic strains vs. time for $\alpha = 3$, $\sigma_1/E = 4 \cdot 10^{-4}$, $\sigma_2/\sigma_1 = 0.5$ and $\psi = 30°$.

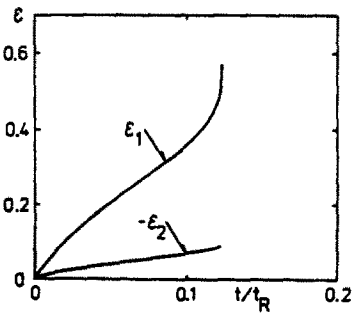

Fig. 6. Average logarithmic strains vs. time for $\alpha = 0$, $\sigma_1/E = 4 \cdot 10^{-4}$, $\sigma_2/\sigma_1 = 0.5$ and $\psi = 30°$.

It may be noted here that a plane strain model analogous to the present axisymmetric model would give quite different results. For a planar, hexagonal array of grains, with micro-cracks formed at all grain facets normal to the maximum principal tensile stress, and with free sliding at the remaining grain boundaries, separation by sliding would occur immediately without any deformation of the grains. Such separation with rigid grains is not possible for the axisymmetric model, which attempts to incorporate some of the geometrical constraints in an actual three-dimensional array of grains.

In Fig. 7 the material is subjected to a uniaxial stress state, $\sigma_1/E = 2 \cdot 10^{-4}$ and $\sigma_2 = 0$, so that the values of the average effective Mises stress σ_e/E and the reference time t_R are unaltered relative to the previous figures. Since $\alpha = 3$ is used in Fig. 7, comparison is made with Fig. 5. The average normal stress $(\sigma_n)_{av}$ in Fig. 7 is half the value of Fig. 5, due to the smaller value of σ_1; but the rupture time is only about 1.5 times larger (not 2^n), because $\sigma_2 = 0$ does not counteract the contraction of the ring. The central grain remains nearly undeformed in the present case, whereas large compressive hoop strains and large axial strains develop in the external ring of material.

The influence of the stress level is considered in Fig. 8, where $\sigma_1/E = 10^{-4}$, $\sigma_2/\sigma_1 = \frac{1}{2}$ and $\alpha = 1$. Thus, all stresses are $\frac{1}{2}$ the values in Fig. 3, all strain-rates are multiplied by 2^{-n}, and the reference time t_R is multiplied by 2^{n-1}. In agreement with this, the creep curves shown in Fig. 8 are indistinguishable from those in Fig. 3, apart from the two times larger values of t/t_R. It is also expected that the other figures shown here are good approximations for stress levels multiplied by a factor k, if the values of t/t_R are divided by k.

In Fig. 9 the influence of the grain geometry is studied, as represented by the cone angle ψ. Here, the stresses are given by $\sigma_1/E = 2 \cdot 10^{-4}$, $\sigma_2/\sigma_1 = \frac{1}{2}$ and $\alpha = 1$, as in Fig. 3; but the geometry differs by the values $R_0/A_0 = 0.417$ and $C_0/A_0 = 0.583$, corresponding to $\psi = 16.1°$. According to (2.16) the average normal stress $(\sigma_n)_{av}$ on the conical grain boundary is increased by a factor of 2 in Fig. 9, relative to Fig. 3, and $\tan\psi$ is reduced by a factor of 2. Then the macroscopic axial strain-rate should increase by a factor of roughly $2^{n+1} = 64$, and the actual increase seen in Fig. 9 is 2 to 3 times this factor. As expected, the value of the angle ψ has a very significant effect on the rate of separation of the grains by grain boundary sliding. Two stages of the sliding process, at $\epsilon_1 = 0.068$ and $\epsilon_1 = 0.447$, are illustrated by the deformed meshes in Fig. 10.

In a number of cases it has been mentioned that some of the differences in the macroscopic strain-rates are connected with differences in the average normal stress $(\sigma_n)_{av}$ on the grain boundary. To get a little more insight in some of the main mechanisms of the problem, a much simplified model has been analysed in the Appendix and compared with the numerical results.

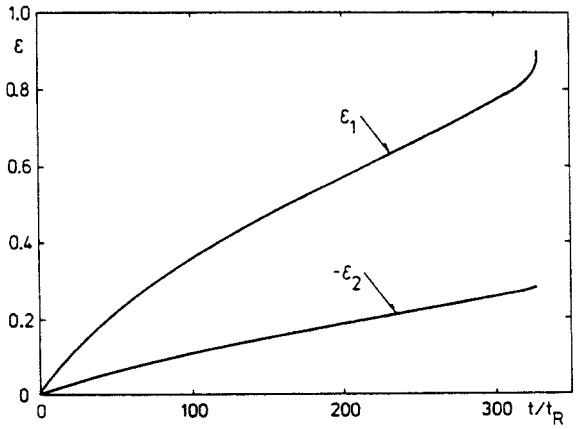

Fig. 7. Average logarithmic strains vs. time for $\alpha = 3$, $\sigma_1/E = 2 \cdot 10^{-4}$, $\sigma_2 = 0$ and $\psi = 30°$.

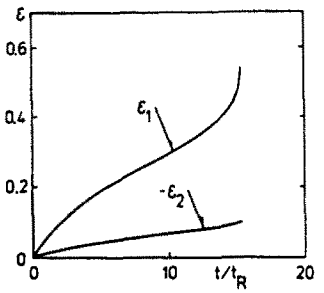

Fig. 8. Average logarithmic strains vs. time for $\alpha = 1$, $\sigma_1/E = 2 \cdot 10^{-4}$, $\sigma_2/\sigma_1 = 0.5$ and $\psi = 30°$.

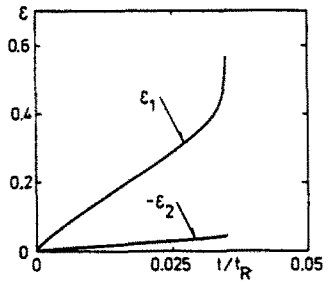

Fig. 9. Average logarithmic strains vs. time for $\alpha = 1$, $\sigma_1/E = 4 \cdot 10^{-4}$, $\sigma_2/\sigma_1 = 0.5$ and $\psi = 16.1°$.

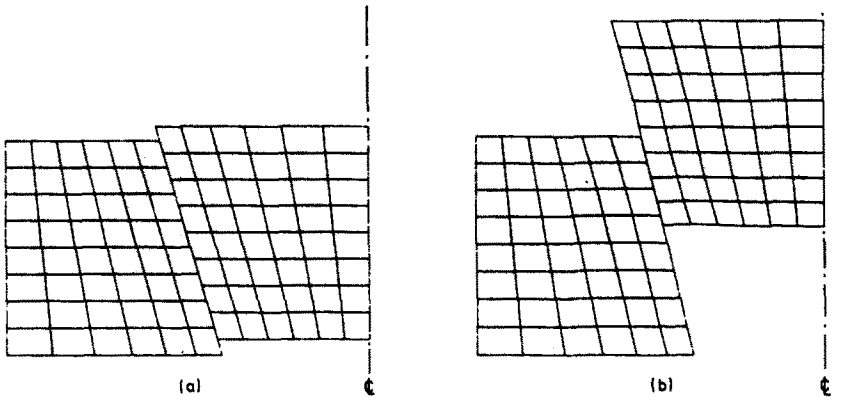

Fig. 10. Deformed meshes corresponding to $\alpha = 1$, $\sigma_1/E = 4 \cdot 10^{-4}$, $\sigma_2/\sigma_1 = 0.5$ and $\psi = 16.1°$. (a) $\epsilon_1 = 0.068$, (b) $\epsilon_1 = 0.447$.

The mode of deformation seen in the previous figures, in which the external ring is pulled in to a significantly reduced radius, can be considered representative of a rather dense population of periodically distributed micro-cracks. However, if the micro-cracks are mainly concentrated near a given plane perpendicular to the x^1-axis, with essentially no cracks at a distance of more than one grain diameter from this plane, large radial contraction-rates are not possible. In such circumstances the overall radial strain-rate will be constrained to equal that in the uncracked material, whereas all the grains along the plane are free to pull apart in the axial direction by grain boundary sliding. To model this situation in a material with prescribed average stresses σ_1 and σ_2, eqn (2.7b) is replaced by the prescribed radial strain-rate

$$\dot{U}_{II}/(A_0 + U_{II}) = -\tfrac{1}{2}\dot{\epsilon}_0(\sigma_e/\sigma_0)^n \tag{4.1}$$

corresponding to the radial creep strain-rate in an uncracked material, with $\sigma_e = |\sigma_1$

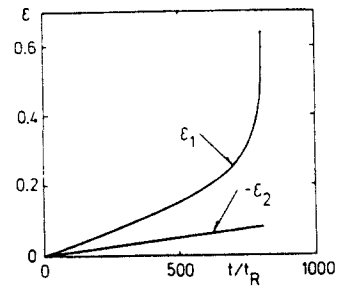

Fig. 11. Average lgarithmic strains vs. time for $\alpha = 3$, $\sigma_1/E = 4 \cdot 10^{-4}$, $\sigma_2/\sigma_1 = 0.5$, $\psi = 30°$ and the special boundary condition (4.1).

$- \sigma_2 |$. In the axial direction the force components still satisfy (2.8), and are related to σ_1 by (2.7a).

In Fig. 11 the condition (4.1) is applied to a material with prescribed average stresses $\sigma_1/E = 4 \cdot 10^{-4}$, $\sigma_2/\sigma_1 = \frac{1}{2}$ and $\alpha = 3$, corresponding to the case considered in Fig. 5. The constant radial strain-rate enforced by (4.1) is about 0.1 times that found in Fig. 5, which increases the rupture time by a factor of 3.7. Two deformed meshes in Fig. 12, at $\epsilon_1 = 0.067$ and $\epsilon_1 = 0.241$, illustrate the somewhat different mode of deformation resulting from the requirement of (4.1). It is seen that radial expansion of the central grain plays a much bigger role here than found in the previous figures.

The condition (4.1) has also been applied for $\alpha = 0$, as shown in Fig. 13. In this case the low radial strain-rate (4.1) increases the rupture time by a factor 6.5, relative to Fig. 6. The average normal stress $(\sigma_n)_{av}$ on the conical grain boundary is four times larger in Fig. 13 than that of Fig. 11. Thus the strain-rates should increase by a factor of roughly $4^n = 1024$. The rupture time found in Fig. 11 is, in fact, about 1000 times larger than that of Fig. 13.

In the last case analysed, an attempt is made to account for some further geometric constraints between the adjoining grains. When the central grain is pulled out of the external ring, the top of this truncated cone has been considered free of any radial forces in the previous calculations, as is seen in Figs. 4, 10 and 12. However, in reality these grains are in contact with other neighbouring grains in a way which is not easily included in the axisymmetric model. The extra constraint on the central grain

$$x^2 + u_2 \leq C_0 + U_{IV}$$
$$1 + \frac{U_{IV}}{C_0} = 1 + \frac{U_{II}}{A_0} \tag{4.2}$$

with the displacement U_{IV} defined in Fig. 14, attempts to model some of these extra limitations on the geometry. The radial surface tractions are integrated over the part

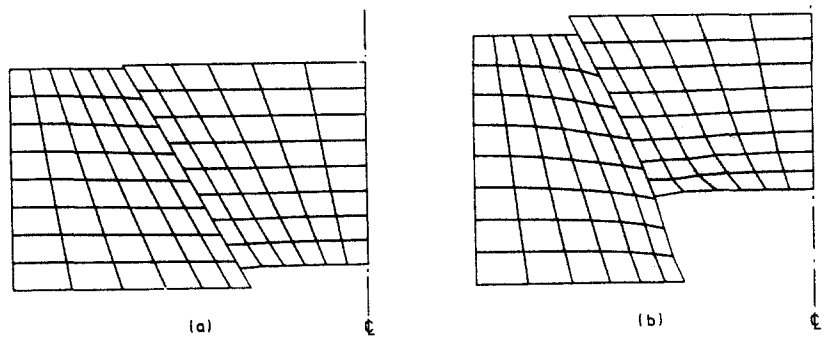

Fig. 12. Deformed meshes corresponding to $\alpha = 3$, $\sigma_1/E = 4 \cdot 10^{-4}$, $\sigma_2/\sigma_1 = 0.5$, $\psi = 30°$ and the special boundary condition (4.1). (a) $\epsilon_1 = 0.067$, (b) $\epsilon_1 = 0.241$.

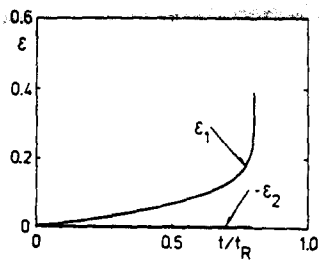

Fig. 13. Average logarithmic strains vs. time for $\alpha = 0$, $\sigma_1/E = 4 \cdot 10^{-4}$, $\sigma_2/\sigma_1 = 0.5$, $\psi = 30°$ and the special boundary condition (4.1).

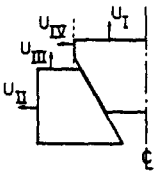

Fig. 14. Mode of deformation with the extra constraint (4.2). The definition of the displacement U_{IV} is indicated.

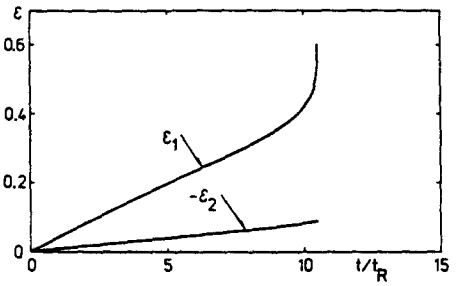

Fig. 15. Average logarithmic strain vs. time for $\alpha = 1$, $\sigma_1/E = 4 \cdot 10^{-4}$, $\sigma_2/\sigma_1 = 0.5$, $\psi = 30°$ and the extra constraint (4.2).

of the central grain surface, where the constraint (4.2) is active, to yield the total radial force component F_{IV}. Furthermore, we here choose to define the average radial stress σ_2 by the expression

$$\sigma_2 = (F_{II} + F_{IV})(2\pi AB)^{-1} \tag{4.3}$$

rather than the expression (2.7b) used above. Apart from (2.7b) the boundary conditions (2.1)–(2.8) are employed.

Figure 15 shows a result obtained with the extra constraint, for stresses $\sigma_1/E = 4 \cdot 10^{-4}$, $\sigma_2/\sigma_1 = \frac{1}{2}$ and $\alpha = 1$, corresponding to the case of Figs. 3 and 4. The effect of the constraint (4.2) is that the top of the central grain is compressed in the radial direction, so that the resulting mode of deformation appears as indicated in Fig. 14, instead of the pattern shown in Fig. 4. It is seen in Fig. 15 that the macroscopic strain-rates are reduced by the constraint, relative to those in Fig. 3, and the rupture time is increased by a factor 1.37.

The macroscopic strain-rates found in the present analyses have been compared with expressions derived by Hutchinson[17], for a creeping solid containing a number of penny-shaped micro-cracks normal to the maximum principal stress. For a high density of penny-shaped cracks, corresponding to a crack at each grain facet normal to the maximum principal stress, the strain-rates are increased by a factor of about 2–4, relative to the uncracked solid. The present axisymmetric model analyses show increases by much larger factors, of the order of 20 for $\alpha = 3$ and 200 for $\alpha = 1$. Thus,

grain boundary sliding adds significantly to the effect of cracks opening, as would be expected.

5. COMPARISON WITH GRAIN BOUNDARY CAVITATION TIMES

The model analyses presented in Section 4 are taken to start at a stage where a micro-crack with radius R_0 has just been formed by coalescence of cavities. The computed times for separation of the grains by grain boundary sliding will be denoted here by t_s. The values of these times found in the present analyses range from $t_s/t_R = 0.035$ in Fig. 9 to $t_s/t_R = 805$ in Fig. 11.

The total failure time also includes the time for nucleation of cavities on the grain boundary facet, and the time for growth of these cavities until coalescence results in the micro-crack. Cavity growth by the interaction of grain boundary diffusion and dislocation creep of the surrounding material has been studied in detail by a number of authors[1, 2, 3], and these growth models have been used to study creep constrained cavitation of grain boundary facets[8, 9]. The time gone from the moment at which the cavities are nucleated until they coalesce is here denoted by t_c, and in the following some t_c values obtained in [9] will be compared with the values of t_s calculated in the present paper.

The rate of diffusive growth of cavities is controlled by the grain boundary diffusion parameter

$$\mathfrak{D} = D_B\delta_B\Omega/kT \tag{5.1}$$

where $D_B\delta_B$ is the boundary diffusivity, Ω is the atomic volume and kT is the energy per atom measure of temperature. Needleman and Rice[1] have represented $\mathfrak{D}$ in terms of a parameter

$$L = (\mathfrak{D}\sigma_e/\dot{\epsilon}_e^C)^{1/3} \tag{5.2}$$

that acts as a stress- and temperature-dependent length scale. Here, σ_e is the effective Mises stress remote from the void, and $\dot{\epsilon}_e^C$ is the corresponding effective creep strain-rate. The voids are assumed to grow in the quasi-equilibrium spherical-caps shape (see [1, 8]), with void radius a and spacing $2b$, so that $(a/b)^2$ is the area fraction of grain boundary which is cavitated. It was shown by Needleman and Rice[1] that the ratio a/L characterizes the growth mechanism, so that diffusion dominates completely for a/L smaller than about 0.1, whereas dislocation creep plays an increasing role for larger a/L values.

The coupled diffusion and creep growth of cavities on a grain boundary facet has been analysed in [9]. Figure 16 shows cavity coalescence times t_c obtained in [9], based on an extension of the model introduced by Rice[8]. This curve is obtained for $a_1/b_1 = 0.1$, $b_1/R_0 = 0.1$, $\sigma_2/\sigma_1 = 0.5$ and $\sigma_1/E = 4 \cdot 10^{-4}$, where $(\,)_1$ denotes the initial value of a quantity. It is seen that t_c/t_R increases significantly for higher values of a_1/L_1. The asymptotic value $t_c/t_R = 118$ in Fig. 16 for small values of a_1/L_1 corresponds to the situation, where growth is entirely constrained by creep. Without this creep constraint, the cavities would grow much faster for small a_1/L_1, and t_c/t_R would approach zero in this range, as shown by Needleman and Rice[1]. The asymptotic value of t_c/t_R, valid in the creep constrained range, is proportional with b_1/R_0 (see Rice[8]) so that more closely spaced cavities relative to the grain size would give shorter growth times.

The normalized times t_c/t_R given in Fig. 16 correspond to $\sigma_1/E = 4 \cdot 10^{-4}$; but Young's modulus affects only the reference time t_R, since the model used to obtain the curve is independent of elasticity. Thus, if all stress levels relative to Young's modulus are multiplied by a factor k, the curve in Fig. 16 is still valid, with t_c/t_R divided by k. Also t_s/t_R is divided by k if the stresses are multiplied by the factor k (see discussion of Fig. 8), so that comparison of t_s and t_c does not depend on the stress level. However, L decreases for increasing stresses according to (5.2), so that the relevant value of the parameter a_1/L_1 increases with the stress level.

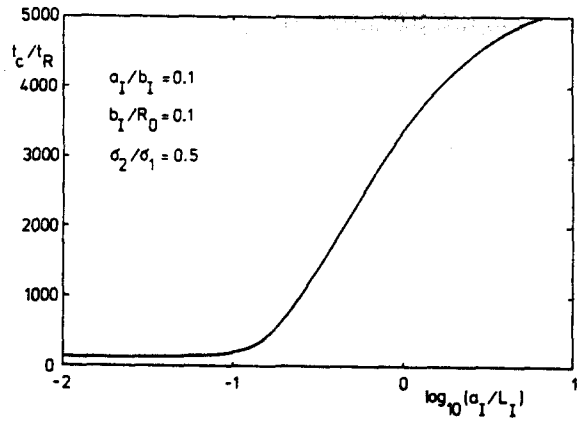

Fig. 16. Times t_c for cavity growth to coalescence on a grain boundary facet, when $\sigma_1/E = 4 \cdot 10^{-4}$. Based on results obtained in [9].

The model used to obtain Fig. 16 does not incorporate sliding on the grain boundaries adjacent to the cavitating grain facet, but inclined to the direction of the maximum principal tensile stress[9]. However, recent computations by the author indicate that free sliding on these adjacent grain boundaries will tend to reduce the growth times t_c by a factor of about $\frac{1}{3}$ to $\frac{1}{4}$ relative to the times given in Fig. 16.

Comparing the cavity growth times t_c in Fig. 16 with the times t_s required for final separation by sliding, it is seen that the final separation process may take a significant part of the total lifetime. This is true if the micro-cracks are rather sparse, so that $\alpha = 3$ (as in Figs. 5 and 11) or even a higher value of α gives the most realistic description by the present model. On the other hand, more closely spaced micro-cracks at grain facets should be better represented by $\alpha = 1$ (as in Figs. 3 or 15), and here it seems that the separation time t_s will be small compared to t_c; dependent on the relevant values of the parameters a_I/L_I, b_I/R_0, etc.

In a real polycrystalline material, cavities will nucleate earlier on some grain boundary facets than others. Likewise some micro-cracks will appear rather early, and subsequently the number of micro-cracks formed by cavity coalescence will keep increasing. The first isolated micro-cracks will open up rather slowly, corresponding to prescribing $U_I = U_{III}$ on the top of the model problem (Fig. 1); but subsequently, as more cracks form, the separation times corresponding to $\alpha = 3$ become relevant. At a final stage, with closely spaced cracks, the calculations for $\alpha = 0$ could represent the rapid separation of the last grains.

The possibility of cavity growth on the sliding grain boundaries inclined to the direction of the macroscopic maximum principal tensile stress has not been discussed so far in the present paper. However, with free grain boundary sliding the normal tensile stresses on the grain boundary are relatively large, and locally these stresses represent the maximum principal stress. The average normal stress (2.16) on the grain boundary ranges from somewhat below to somewhat above the prescribed stress σ_1 in the cases considered here, and the relevant cavity growth times should be represented by curves analogous with that of Fig. 16. Somewhat shorter growth times than those in Fig. 16 would be expected for small values of a_I/L_I, though, since the given average stress (2.16) on the inclined grain boundaries leaves less possibility of a creep constraint on cavity growth.

For relatively large values of a_I/L_I, say larger than 0.33, and still assuming $a_I/b_I = 0.1$ on the sliding grain boundaries, the order of magnitude of the cavity growth times shown in Fig. 16 indicates that the separation of grains by grain boundary sliding will occur faster than cavity coalescence on the sliding boundaries. However, for small a_I/L_I, say smaller than 0.1, the cavity growth is so rapid that the time to coalescence on the sliding grain boundary can be much shorter than the time t_s required for separation by sliding. A more precise comparison would require an analysis of the interaction

between sliding and cavity growth on the sliding grain boundaries; but the present considerations give at least an indication. Thus, it can be expected that the computed separation times t_s are mainly relevant in the regime where dislocation creep gives a noticeable contribution to cavity growth, as is often the case at relatively high stress levels. In the regime where diffusional cavity growth dominates completely, much smaller separation times should be expected than those predicted by sliding alone.

If the viscosity in the sliding grain boundaries was not neglected, as has been done in the present analyses, the separation times t_s would be higher than the values calculated here. Also the cavity growth times t_c for a grain boundary facet normal to the maximum principal stress would increase, and the same effect is expected for cavity growth times on the sliding grain boundaries, since the non-zero shear stresses on these interfaces will reduce the normal stresses. Thus, incorporating a grain boundary viscosity would be expected to increase all parts of the total failure time discussed here.

REFERENCES

1. A. Needleman and J. R. Rice, Plastic creep flow effects in the diffusive cavitation of grain boundaries. *Acta Metallurgica* **28**, 1315–1332 (1980).
2. A. C. F. Cocks and M. F. Ashby, On creep fracture by void growth. *Prog. Mat. Sci.* **27**, 189–244 (1982).
3. T.-L. Sham and A. Needleman, Effects of triaxial stressing on creep cavitation of grain boundaries. *Acta Metallurgica* **31**, 919–926 (1983).
4. D. Hull and D. E. Rimmer, The growth of grain-boundary voids under stress. *Phil. Mag.* **4**, 673–687 (1959).
5. W. A. Trampczynski, D. R. Hayhurst and F. A. Leckie, Creep rupture of copper and aluminium under non-proportional loading. *J. Mech. Phys. Solids* **29**, 353–374 (1981).
6. B. F. Dyson, A. K. Verma and Z. C. Szkopiak, The influence of stress state on creep resistance: Experiments and modelling. *Acta Metallurgica* **29**, 1573–1580 (1981).
7. B. F. Dyson, Constraints on diffusional cavity growth rates. *Metal Science* **10**, 349–353 (1976).
8. J. R. Rice, Constraints on the diffusive cavitation of isolated grain boundary facets in creeping polycrystals. *Acta Metallurgica* **29**, 675–681 (1981).
9. V. Tvergaard, On the creep constrained diffusive cavitation of grain boundary facets. *J. Mech. Phys. Solids* **32**, 373–393 (1984).
10. M. F. Ashby, Boundary defects, and atomistic aspects of boundary sliding and diffusional creep. *Surf. Sci.* **31**, 498–542 (1972).
11. F. A. McClintock and A. S. Argon, *Mechanical behaviour of materials*. Addison-Wesley Publishing Company (1966).
12. F. W. Crossman and M. F. Ashby, The non-uniform flow of polycrystals by grain-boundary sliding accommodated by power-law creep. *Acta Metallurgica* **23**, 425–440 (1975).
13. F. Ghahremani, Effect of grain boundary sliding on steady creep of polycrystals. *Int. J. Solids Structures* **16**, 847–862 (1980).
14. F. K. G. Odqvist, Non-linear solid mechanics, past, present and future. *Proc.* 12th *Int. Congr. Appl. Mech.* (Edited by M. Hetényi and W. G. Wincenti), pp. 77–99. Springer Verlag (1969).
15. D. Peirce, C. F. Shih and A. Needleman, A tangent modulus method for rate dependent solids. *Comput. Structures* **18**, 875–887 (1984).
16. V. Tvergaard, Influence of voids on shear band instabilities under plane strain conditions. *Int. J. Fracture* **17**, 389–407 (1981).
17. J. W. Hutchinson, Constitutive behaviour and crack tip fields for materials undergoing creep-constrained grain boundary cavitation. *Acta Metallurgica* **31**, 1079–1088 (1983).

APPENDIX

A much simplified version of the model problem illustrated in Fig. 1, with the boundary conditions (2.1)–(2.8), will be analysed here. The purpose is to try to extract some of the main mechanisms of the numerical model.

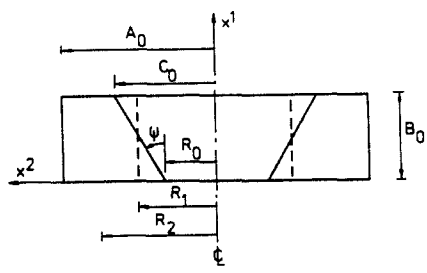

Fig. A1. External ring and central cylinder in contact at radius R_1, as assumed in the simplified model.

The model in the initial stage is analysed here as a central cylinder, with radius $R_1 = (R_0 + C_0)/2$, and a ring with mean radius $R_2 = (R_1 + A_0)/2$; see Fig. A1. Both in the cylinder and the ring, uniform stress states are assumed, representing averages of the actual stress distributions, and the corresponding creep strain-rates are found. Finally, the radial displacement rates on the surfaces with radius R_1 are used to determine the rate of sliding on the actual grain boundary with the angle of inclination ψ.

The specified average stresses are σ_1 and σ_2, and the relation $\sigma_1 = F_1(1 + \alpha)(\pi A_0^2)^{-1}$ follows from (2.7a) and (2.8). The normal tensile stress σ_b on the inside of the ring and on the outside of the cylinder is the average effect of the radial component of the force transmitted over the grain boundary. The result is

$$\sigma_b = (\sigma_n)_{av} \tag{A.1}$$

where the average normal stress $(\sigma_n)_{av}$ on the actual, conical grain boundary is given by (2.16).

The uniform stress state assumed in the central cylinder is

$$\sigma_1^C = \frac{1}{2}\frac{F_1}{\pi R_1^2}, \qquad \sigma_2^C = \sigma_3^C = \sigma_b. \tag{A.2}$$

From these stresses the values of the stress deviators s_i^C and the Mises stress σ_e^C are determined, and the corresponding strain-rates are

$$\dot{\epsilon}_i^C = \tfrac{3}{2}\dot{\epsilon}_0(\sigma_e^C/\sigma_0)^{n-1}s_i^C/\sigma_0, \qquad \text{for } i = 1, 2, 3. \tag{A.3}$$

In the ring the axial stress is taken to be the average of that at the top and that at the bottom, the radial stress is taken as the average of those at the inner and outer radii, and the circumferential stress is given by equilibrium

$$\sigma_1^R = \left(\frac{1}{2} + \alpha\right)\frac{F_1}{\pi(A_0^2 - R_1^2)}, \quad \sigma_2^R = \frac{\sigma_b + \sigma_2}{2}, \quad \sigma_3^R = \frac{\sigma_2 A_0 - \sigma_b R_1}{A_0 - R_1}. \tag{A.4}$$

In terms of the corresponding stress deviators s_i^R and Mises stress σ_e^R, the strain-rates $\dot{\epsilon}_i^R$ are given by expressions analogous with (A.3).

Now, with the approximations made above, the radial displacement-rates on the outside of the cylinder and the inside of the ring, respectively, are

$$\dot{u}^C = R_1\dot{\epsilon}_2^C, \quad \dot{u}^R = R_2\dot{\epsilon}_3^R - \tfrac{1}{2}(A_0 - R_1)\dot{\epsilon}_2^R \tag{A.5}$$

and the external displacement-rates, defined in (2.3) and (2.4), are

$$\dot{U}_I = (\dot{u}^C - \dot{u}^R)/\tan\psi + \frac{B_0}{2}(\dot{\epsilon}_1^R + \dot{\epsilon}_1^C) \tag{A.6}$$

$$\dot{U}_{II} = R_2\dot{\epsilon}_3^R + \tfrac{1}{2}(A_0 - R_1)\dot{\epsilon}_2^R. \tag{A.7}$$

In Table A1 the macroscopic strain-rates $\dot{\epsilon}_1 = \dot{U}_I/B_0$ and $\dot{\epsilon}_2 = \dot{U}_{II}/A_0$, predicted by this simple model, are compared with the numerical results obtained in Section 4, for all cases in which the same boundary conditions (2.1)–(2.8) are employed. The numerically found strain-rates decay in the initial stage, as has been discussed in Section 4; but the values after a small amount of straining, $\epsilon_1 = 0.02$, are chosen in Table A1. At this small strain the initial geometry is still well approximated, while most elastic stress peaks seem to have been relaxed. The numerical results in Table A1 are rather well represented by the simple model in all cases. Thus, it seems that the simple model can be used to obtain a rough estimate of the creep-rates to be expected. It should be noted, though, that the strain-rates found numerically drop to values around or less than half of those shown in the table, at somewhat larger strains.

In order to check the influence of various terms it has been tried to only include the first terms on the right-hand-sides of eqns (A.5b), (A.6) and (A.7). For the case of Fig. 3 this reduces $\dot{\epsilon}_1$ by a factor 0.78 and increases $|\dot{\epsilon}_2|$ by a factor of 1.2. As would be expected, the first term in (A.6) plays a central role in representing the effect of the grain boundary sliding.

	Simple model		Numerical result at $\epsilon_1 = 0.02$	
	$\dot{\epsilon}_1 t_R$	$-\dot{\epsilon}_2 t_R$	$\dot{\epsilon}_1 t_R$	$-\dot{\epsilon}_2 t_R$
Fig. 3	0.139	0.030	0.120	0.027
Fig. 5	0.00456	0.00131	0.00424	0.00126
Fig. 6	7.53	1.44	6.13	1.20
Fig. 7	0.00654	0.00170	0.00609	0.00159
Fig. 8	0.0699	0.0152	0.0598	0.0132
Fig. 9	17.3	1.76	14.7	1.51

Table A1. Initial strain-rates from simple model compared with numerical results.